Landslides (2013) 10:503–513
DOI 10.1007/s10346-013-0400-x
Received: 6 February 2013
Accepted: 28 March 2013
Published online: 2 May 2013

Guoquan Wang · James Joyce · David Phillips · Ramesh Shrestha · William Carter

Delineating and defining the boundaries of an active landslide in the rainforest of Puerto Rico using a combination of airborne and terrestrial LIDAR data

Abstract Light detection and ranging (LIDAR) is a remote sensing technique that uses light, often using pulses from a laser to measure the distance to a target. Both terrestrial- and airborne-based LIDAR techniques have been frequently used to map landslides. Airborne LIDAR has the advantage of identifying large scarps of landslides covered by tree canopies and is widely applied in identifying historical and current active landslides hidden in forested areas. However, because landslides naturally have relatively small vertical surface deformation in the foot area, it is practically difficult to identify the margins of landslide foot area with the limited spatial resolution (few decimeters) of airborne LIDAR. Alternatively, ground-based LIDAR can achieve resolution of several centimeters and also has the advantages of being portable, repeatable, and less costly. Thus, ground-based LIDAR can be used to identify small deformations in landslide foot areas by differencing repeated terrestrial laser scanning surveys. This study demonstrates a method of identifying the superficial boundaries as well as the bottom boundary (sliding plane) of an active landslide in National Rainforest Park, Puerto Rico, USA, using the combination of ground-based and airborne LIDAR data. The method of combining terrestrial and airborne LIDAR data can be used to study landslides in other regions. This study also indicates that intensity and density of laser point clouds are remarkably useful in identifying superficial boundaries of landslides.

Keywords Airborne LIDAR · GPS · Landslide · Rainforest · TLS

Introduction

Landslides are the major geological hazard in Puerto Rico, as well as in the whole Caribbean region. Mountainous terrain and tropical climate combine to make the island one of the most landslide-prone areas in the USA. An active landslide in El Yunque National Rainforest, Puerto Rico, was investigated in this study. The landslide is located on a steep, north-facing mountain slope in rainforest. Major displacements of the landslide in 2004 and 2005 blocked one of three access roads to the national park. In order to reopen the roadway (Puerto Rico 9966), a 100-m-long steel sheet-piling wall was designed and constructed to restrain the landslide (Fig. 1). During construction, a portion of the west end of the wall failed. The failure was attributed to insufficient depth of the support steel piles. The retaining wall was rebuilt with the depth of the support steel piles having been doubled. The reconstruction was finally completed at the end of 2009. However, the previously failed section continued to show slope and flexural deformation over the spring and summer of 2010 and finally ruptured in July of 2010, during a heavy rainfall (Fig. 1, bottom). As a result, the road was not reopened. The other two access roads also suffer from frequent small-scale landslides and rockfalls. The loss of the road is a major concern to EL Yunque National Rainforest administration and the local government.

The failure of the retaining wall implies that the size of the landslide was larger than the size estimated by the designers of the retaining wall. However, the significant deformation area of the retaining wall was limited to a small section, about 10-m wide (Fig. 1). This suggests that the future motion of landslide might still be retained by proper engineering design and construction. Therefore, identifying the true extent and depth of the landslide has become the key issue for taking further actions. However, landslides occurring under steep and thickly forested areas are difficult to map with conventional methods. Limited visibility and difficult access reduce the area that can be directly observed using standard aerial photography, satellite imagery, or ground-based surveys.

During the past decades, light detection and ranging (LIDAR) technology has been widely used in different disciplines, such as archaeology, geography, geology, geomorphology, seismology, forestry, atmospheric physics, airborne laser swath mapping, and laser altimetry (Wehr and Lohr 1999; Shan and Toth 2008). Laser scanning was developed in three ways, depending on the position of the sensor: terrestrial laser scanning (TLS), airborne laser scanning (ALS), and satellite-based laser scanning (Carter et al. 2007). High-resolution digital elevation maps derived from ALS data have led to many novel studies in geoscience applications (e.g., Falls et al. 2004; Bevis et al. 2005; Glenn et al. 2005, 2006; Wooten et al. 2007; Delano and Braun 2007). ALS has been frequently applied in regional landslide mapping, modeling, monitoring, and risk assessment in many parts of the word. The ability of ALS to measure the land surface elevation beneath vegetated canopy has significantly advanced landslide studies where the terrain is forested (e.g., Van den Eeckhaut et al. 2007; Razak et al. 2011). In these studies, high-resolution digital terrain models (DTMs), also called 3D "bare-earth models," derived from ALS data served as the base data set for creating topographic maps and for identifying landslide scarps.

TLS, also referred to as ground-based LIDAR, appeared at the end of the 1990s (Heritage and Large 2009). TLS has frequently been applied to the study of small-scale landslides in the last 5 to 10 years, particularly in studying active landslides (e.g., Abellan et al. 2006, 2009; Teza et al. 2007, 2008; Travelletti et al. 2009; Corsini et al. 2009; Dunning et al. 2009; Jaboyedoff et al. 2009; Kasperski et al. 2010; Wang et al. 2011; Fanti et al. 2012). TLS surveys allow researchers to generate detailed models of a landslide surface. When two or more georeferenced digital surface or terrain models obtained by multiple TLS surveys are available, the volume change of sliding mass, the margins of the deformation area, and the landslide displacement field, can be computed. Thus, TLS is particularly useful in detecting the margins of creeping landslides.

The number of publications discussing the use airborne and ground-based LIDAR in landslide studies has grown considerably during the last decade (Derron and Jaboyedoff 2010). Jaboyedoff et

Fig. 1 Panorama views at the landslide site taken on 25 May 2010 and 5 February 2011 during the first and third TLS surveys, respectively. Note that the panorama view was slightly distorted. The wide-angle landscape was assembled with four narrow-angle photos taken by the digital camera on the ground-based LIDAR scanner using a free photo stitching software (http://hugin.sourceforge.net)

al. (2012) gave a comprehensive review of applications of ALS and TLS in landslide studies. The majority of ALS applications in landslide studies were limited to the detection of landslide scarps based on hillshades of DTMs derived from ground returns (e.g., Carter et al. 2001; Haugerud et al. 2003; Ardizzone et al. 2007; Jaboyedoff et al. 2008; Booth et al. 2009; Corsini et al. 2009). Landslides naturally have large vertical deformation in the head areas and insignificant vertical deformation in the foot areas, particularly in the toe areas. The elevation accuracy of airborne LIDAR data is typically at the level of a couple of decimeters for large-scale mapping applications (e.g., Adams and Chandler 2002; Bowen and Waltermire 2002; Hodgson et al. 2003; Habib 2008). As a result, it is difficult to identify margins in landslide foot area from DTM models derived from ALS data. Fortunately, foot areas of landslides are often located in downslope areas of hills with possible ground access, such as along road cuts. So TLS is often feasible to map foot areas of landslides. In this paper we describe the combination of TLS, ALS, and Global Positioning System (GPS) data to identify superficial boundaries as well as the basal failure plane of an active landslide in a rainforest.

Airborne LIDAR surveying and data processing

The airborne LIDAR scanning was performed by the National Center for Airborne Laser Mapping (NCALM, http://www.ncalm.org) during 13–16 May 2011. This survey was performed with an Optech Gemini Airborne Laser Terrain Mapper (serial number 09SEN185, http://www.optech.ca) mounted in a twin-engine Cessna 337 Skymaster aircraft. The Optech Gemini model is capable of laser pulse rates up to 167 kHz. It records as many as four returns (including the first three and last) per shot and has a switchable beam divergence of 0.25 and 0.80 milliradians. The data were collected at flying heights of 600 m with 50 % overlap between adjacent flight lines. The laser beam divergence was switched to 0.80 milliradians, which led to a spot size of 0.48 m in diameter on the ground at 600 m flying height. Simultaneous acquisition of aircraft position and orientation was performed using a combination of differential kinematic GPS and Inertial Navigation System (INS). Ground coordinates of laser points were calculated by combining information from the scanner, GPS/INS measurements, and calibration parameters.

Removing trees and vegetation, or identifying "bare-earth" returns, is the primary focus of the data processing for this project. A commercial software package, TerraSolid's TerraScan (http://www.terrasolid.fi), was used to classify the raw laser point into three categories: ground, nonground (default), and artifacts (aerial/isolated points and multi-path points). An automatic ground classification procedure, specifically a TerraScan macro, was performed initially, and then a manual process, "add point to ground," was conducted to correct classification errors in areas where the automatic ground classification did not provide a good result. The main purpose of the manual process is to retain sufficient details of the bare-earth surface, while removing low vegetation and tree trunks. Particular attention is paid to the segmentation of points near sharp topographic features, such as head scarps and flanks of the landslide, where it is often possible to classify ground returns to non-ground returns due to the pronounced topographic gradient.

Density and intensity of point clouds

Figure 2 shows point clouds hit on the flat surface (14×4 m) of a black asphalt road in front of the retaining wall. The ALS point density on the black road surface is about 10 points/m^2. The standard deviation of elevation measurements is 22 cm. The point density in the deforested foot area is slightly higher than that of the black road surface. However, the overall return point density was almost doubled inside the rainforest due to multiple returns from tree canopies and undergrowth. Up to four laser returns were collected for laser pulses in the dense canopy area as shown in Fig. 3. Figure 4 (left) shows the sparse and uneven distribution of ground returns. Ground-point spacing can be larger than 5 m

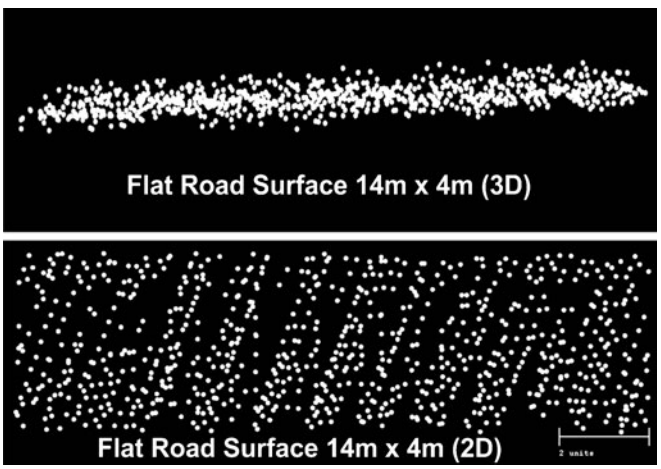

Fig. 2 Airborne LIDAR point clouds hit on the flat black asphalt road surface in front of the landslide. The point density is 10 points/m^2. The standard deviation of vertical coordinates of these points is 21 cm. The unit of the scale in the bottom figure is meter

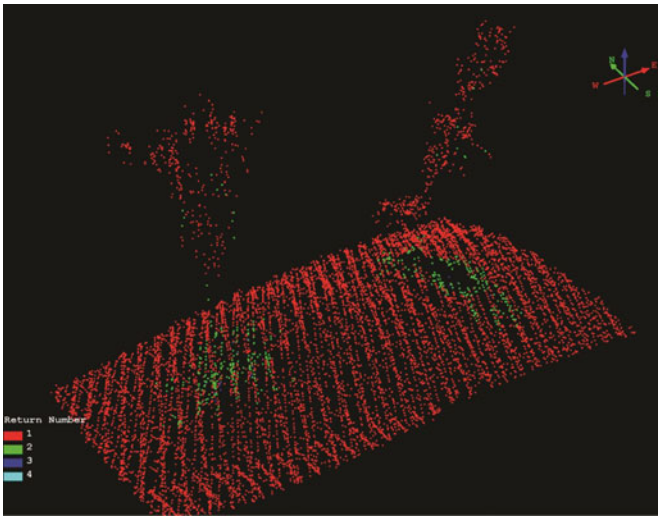

Fig. 3 Multiple returns collected by airborne LIDAR in a tree canopy covering area. These two trees are located at the top of the graded landslide foot area (see Figs. 1 and 8)

under tree canopies. The average point density inside the forest is about 1 point/3 m^2. However, there are considerably dense ground returns along head scarps and both eastern and western flanks. This is due to the fact that trees were felled and displaced along the margins of the moving mass and soil was exposed. As a result, a large number of laser points directly hit the ground surface along the head scarps and two flanks, highlighting the boundary in landslide head and body areas.

LIDAR systems provide both elevation and intensity records for each laser return. LIDAR intensity, a relative measure of the strength of each return pulse, in theory, is determined by an object's reflectance. Intensity values can be used to identify land-cover classes when the data are carefully calibrated (e.g., Donoghue et al. 2007). Previous investigations have indicated that LiDAR intensity values also depend on atmospheric transmission, local incidence angle, surface roughness, laser beam divergence, and sensor-to-object distance (e.g., Hodgson and Bresnahan 2004; Mazzarini et al. 2007; Hasegawa 2006; Shrestha et al. 2007). In general, LIDAR intensity is predominantly dependent on sensor-to-object distance and subordinately dependents on local incidence angle (e.g., Kaasalainen et al. 2005) and atmospheric absorption (e.g., Mazzarini et al. 2007). Mazzarini et al. (2007) reported that intensity level changes with the inverse square of the distance. While intensity calibrations for the terrain's directional spectral properties remain an open area of LIDAR research, normalization of intensities based on sensor-to-object is fairly straightforward to implement. In standard NCALM data processing, the original intensities are normalized with the sensor-to-object path lengths (Shrestha et al. 2007). Figure 4 (right) illustrates the normalized intensities of ground returns. The differences of intensities are mostly caused by the change of surface material types. The high intensities (white) were returned from soil while lower intensities (gray) were returned from trees and vegetation.

The laser density and intensity images shown in Fig. 4 clearly delineate the margins of the landslide flanks and head area. Furthermore, these images also define three distinctive portions of the main landslide. The uppermost portion (head) is characterized by very low point cloud density and intensity, which indicates that the forest remains largely intact. The landslide here is behaving as a largely coherent slide mass with little deformation occurring at the surface. In contrast to this, the middle portion (body) of the landslide is characterized by a very patchy distribution of point cloud density and intensity indicating significant disruption of the trees by ground surface deformation. The distribution of the higher density and intensity point clouds is notably arc shaped suggesting the occurrence of secondary scarps in this portion of the landslide (Fig. 4). The bottom (foot and toe) of the landslide is characterized by high density and intensity point clouds as a consequence of the removal of the vegetation and tree cover during earthwork and grading for the construction of the retaining wall (see Fig. 1).

Accuracy of ALS data

The error budget for a given ALS is primarily driven by errors from the laser source, the laser rangefinder, the kinematic GPS position solution, the INS orientation solution, environmental conditions, land-cover category, and errors involved in post-data processing. Most vendors quote 15–18 cm vertical accuracy and 0.5 m horizontal accuracy. Vertical accuracy under 10 cm and

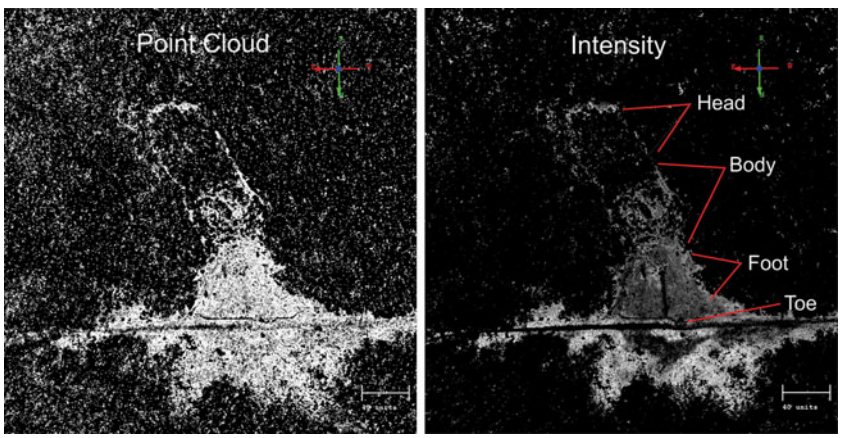

Fig. 4 Images showing 2D distribution of ground returns (point clouds) collected by ALS and their intensities. The margins in the landslide head and body areas can be identified from both point cloud density and intensity images. The unit of the scale in both figures is meter

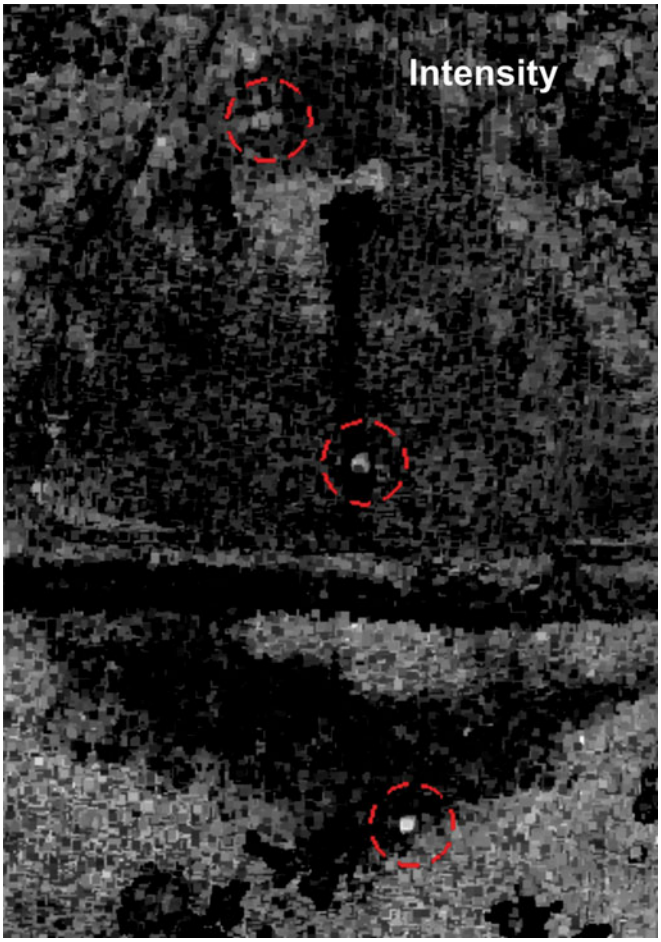

Fig. 5 Intensity map of total airborne LIDAR returns showing places of three ground targets placed in the field during airborne LIDAR survey

horizontal accuracy within 30 cm are often expected for most NCALM data products (Shrestha et al. 1999, 2007; Slatton et al. 2007). In order to check the accuracy of airborne LIDAR, we placed three ground targets in the landslide area during the airborne LIDAR survey period, which can be identified from the intensity map of whole point clouds (Fig. 5). The ground targets had a white coating that provided substantially different reflectance than their surroundings. Figure 6 (left) shows the ground target in the middle of the landslide foot area. The GPS receiver, which was not on the table during ALS surveying, was used to measure coordinates of the center of the table. We selected 11 bright points with large intensity values to represent the returns from the table surface (Fig. 6, right). It is difficult to identify ground targets with elevations of point clouds. The height and diameter of the table is 0.8 and 1.2 m, respectively. Table 1 lists the comparisons of table centers inferred from point clouds and GPS antennas. The differences, also called accuracy, between the centers inferred from leaser points and measured by GPS are within 25 cm vertically and 40 cm horizontally. The standard deviations (1σ), also called precision, of vertical coordinates of laser points from ground targets are within 20 cm, which is comparable with the vertical precision (22 cm) inferred from a large number of laser points hit on the flat road in front of the retaining wall (Fig. 2). The steep topography likely affected the accuracy of point clouds. Table 1 also indicates that all three vertical coordinates of the centers of the ground targets as inferred from ALS data are lower than those inferred from GPS measurements, which might imply the occurrence of a systematic vertical error in the ALS data set. In summary, the vertical precision or repeatability of ALS point clouds collected in this study is about 20 cm, whereas accuracy in vertical and horizontal components are within 25 and 40 cm, respectively.

Figure 7 shows the DTM and digital surface model (DSM) of the landslide area derived from ALS data. The headscarps and flanks of landslides are well defined on the DTM. Details of the different portions of the head on the DTM are indicative of recent activity and are strikingly accurate portrayals of what was observed during the geologic surveys. However, the lower flank boundaries of the current sliding mass in the deforested area are hardly seen because of the insignificant changes in ground elevations, despite the considerably high point cloud density (about 12 points/m^2). The lack of lower flank escarpments is typical of mass movements that change from translational landslides to earth flows in their foot and toes.

TLS data acquisition, processing, and accuracy

Three TLS campaign surveys were conducted in the landslide foot area from 24 to 25 May 2010, 23 to 24 August 2010, and 5 to 6 February 2011. A Riegl VZ-400 laser scanner (http://www.riegl.com) was used to collect TLS data in the field. This scanner provides high resolution, high-speed, 3D data acquisition using a narrow infrared laser beam and a fast scanning mechanism. The range of the scanner is up to 600 m with a point

Fig. 6 Images showing the ground target in the middle of Fig. 5 and the laser points hit on the surface of the ground target. Note that the GPS antenna and rocks were not on the table during the airborne LIDAR surveying period. The unit of the scale in the right figure is meter

Table 1 Comparisons of the centers of ground targets inferred from ALS data and GPS measurements

Ground targets	Point clouds hit on the surface of ground targets				Average coordinates (m)[b]			GPS antenna[a] Coordinates (m; 16 May 2011)			Accuracy Point clouds-GPS (cm)		
	Number of points	Standard deviation (cm)											
		EW	NS	UD	EW	NS	UD	EW	NS	UD	EW	NS	UD
Low target	11	16.7	33.4	7.7	206,409.545	2,029,169.257	437.435	206,409.2	2,029,169.18	437.669	34.5	7.7	−23.4
Middle target	11	32.9	30.9	14.6	206,416.666	2,029,125.412	448.711	206,416.482	2,029,125.44	448.793	18.4	−3.1	−8.2
High target	11	43.6	47.5	16.4	206,429.605	2,029,083.961	459.411	206,429.823	2,029,084.05	459.681	−21.8	−8.4	−27

[a] The vertical coordinate of each GPS antenna had been adjusted to the surface of the ground target

[b] The positions of point clouds and GPS are tied to North America Horizontal Datum of 1983 (NAD83 and CORS96) and North America Vertical Datum of 1988 (NAVD88 and GEOID03). The horizontal projection is UTM NAD83 Zone 20 N

Fig. 7 DSM (*outer part*) and DTM (*inner part*) derived from airborne LIDAR data

acquisition rate of up to 122,000 measurements/s. The scanner is able to acquire a scene with a field of view of up to 360° horizontal and 100° vertical in a single scan. The Riegl scanner has an integrated digital compass for accurate north-determination of the direction for polar alignment of the Scanner's Own Coordinate System (SOCS). A digital camera (NIKON D700) was mounted on the top of the scanner. The camera was configured to take 6 photos in a 360° view automatically at the end of each single scan. The camera coordinate system was aligned to the intrinsic reference system (SOCS) of the scanner. All the data collected in the field by the terrestrial scanner and camera are managed by the companion software Riscan PRO (Version 1.6.3). The images were later registered to the laser scanner data and used as a texture source in the photorealistic virtual model.

TLS data acquisition

Figure 8 shows point clouds collected during the first TLS campaign survey in May 2010. The point clouds were colored with true color obtained from photos taken with the digital camera. The white point clouds represent places that were not caught by the digital camera. The complete coverage of spatially complex objects by TLS can only be guaranteed, if data collection is done from different viewpoints. We conducted more than ten single scans

Fig. 8 Colored point clouds collected by TLS (RIGEL VZ-400) on 25 May 2010 during the first TLS survey

during each TLS campaign survey from different viewpoints located inside and outside of the landslide foot area. The locations of these single scans were carefully selected to capture the complete surface geometry of the graded area. Ten reflective targets (control points) were placed in the landslide area during the TLS survey. We also installed three GPS stations in the study area during each TLS campaign survey. GPS0 is outside of the landslide area beyond the toe. GPS2 and GPS1 are in the high and low parts of the landslide foot area, respectively (see Fig. 11). Three GPS stations were continuously operated during each TLS survey period. OPUS, a free on-line GPS data processing service provided by NGS (www.ngs.noaa.gov/OPUS), was used to calculate the global positions of these three GPS antennas (over 8 h). According to our recent study (Wang and Soler 2012), horizontal accuracy of 1 cm and vertical accuracy of 2 cm are achievable for 8-h or longer sessions in Puerto Rico. Three reflectors were co-located with these GPS antennas (Fig. 9). Each single-scan has its own local coordinate system (SOCS) and could identify at least four reflectors in the field. RISCAN Pro was used to register all single scans to a common reference frame, called project coordinate system (PRCS). We used the SOCS assigned by the scanner to the first scan position as the PRCS for each campaign survey. The registration errors, root mean error square (RMES), were less than 2 cm for all registrations. The overall registration was refined based on independent measurements from these three GPS units. The PRCS coordinate system was transferred to a global coordinate system using GPS coordinates. The RMSE generated during the coordinate transformation was less than 3 cm. The density of point clouds in the landslide area varied considerably. Most areas were scanned more than three times; some were only scanned once. The shadow-masked zones (dark holes) in Fig. 8 were not scanned because of irregular topography. Figure 10 shows point clouds of a segment of flat surface of the black asphalt road in front of the landslide. The left edge shows the density as high as 40 points within a 5×5 cm area, which were scanned five times, while the right part shows the density of 1 to 2 points within an area of the same cell size, which were scanned only once. The majority of the deforested landslide foot area was scanned more than three times and the point density was higher than 5 points/25-cm^2 cell.

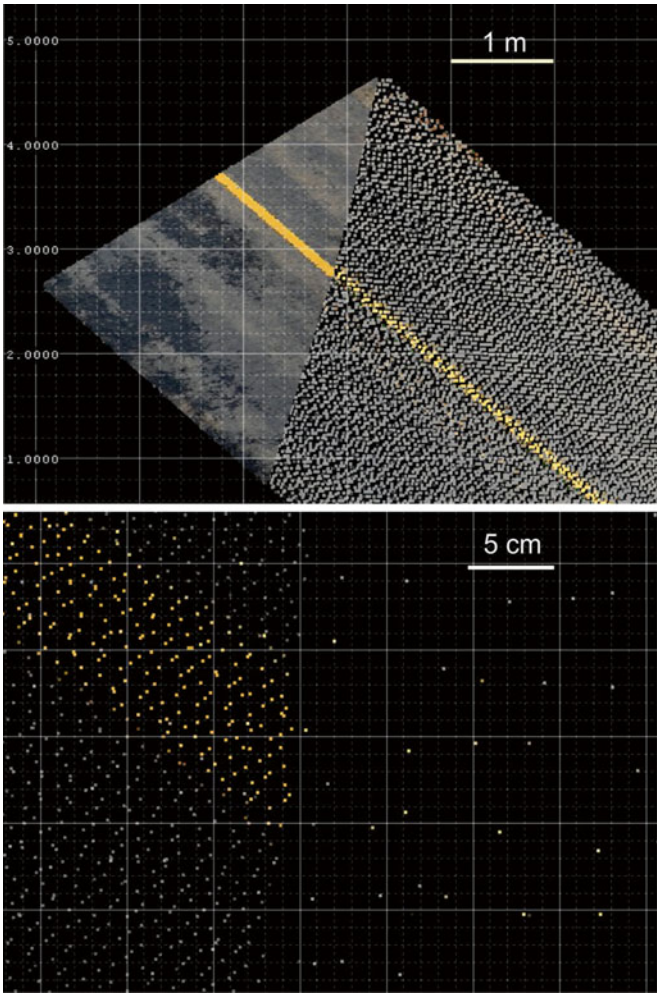

Fig. 10 The top map shows TLS point clouds hit on a piece of flat black asphalt road surface (5×6 m) in front of the retaining wall. The bottom map is a zoomed in view of the *red rectangle* area in the top map. The point density was about 40 points/25 cm^2 (5×5 cm cell) in the left side and 1 to 2 points/25 cm^2 in the right side. The left side was scanned five times from different scan positions

Accuracy of TLS data

The raw data product of a laser scan survey is a three-dimensional (3D) point cloud, a common coordinate system in which each data point has *X* (easting), *Y* (northing), and *Z* (relative height) values, intensity, and red, green, and blue color values. According to the estimation from the vendor, Riegl VZ-400 achieves precision and accuracy at the level of 3 and 5 mm, respectively. Precision indicates the degree to which further measurements show the same result, also called reproducibility or repeatability. The standard deviation (1σ) of a group of samples collected on a surface at 100-m range is used as the value of precision by vendors. About 68 % of the samples will fall within the limit. Accuracy is defined as the degree (one sigma at 100 m range) of conformity of a measured quantity to its true position. Nevertheless, the precision and accuracy given by manufacturers were obtained under ideal conditions. The instrumental accuracy is usually lower in practical applications due to unfavorable conditions such as: poorly reflective or very rough surfaces, bad weather conditions (e.g., rain drops, hot wind, or fog), very bright ambient conditions, parallel incident angles, excessive range, etc. We checked the point-to-point distance between each two reflectors collocated with GPS. The differences of the distance measured by point clouds and GPS

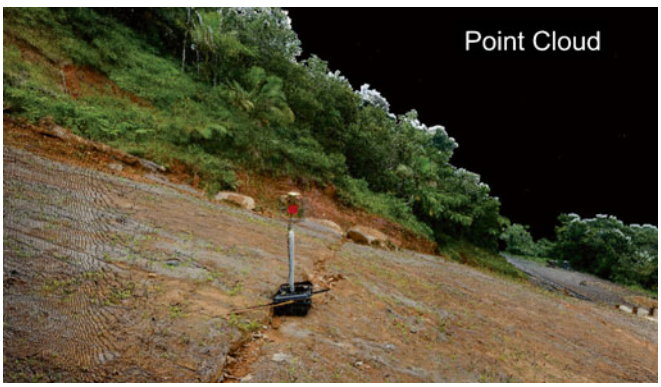

Fig. 9 Colored TLS point clouds showing a pair of collocated GPS antenna and reflector (*red round panel*) installed for TLS survey

are within 3 cm for all three TLS campaign surveys. We cut a piece of flat road surface (14×4 m) in front of the road to study the vertical precision (repeatability) of laser returns. There were about 98,000 points (1,500 points/m²). The standard deviation (σ) of vertical measurements of these points was 2 cm.

The point cloud from each single scan was exported as ASCII data using the Riscan Pro software. These data points were unevenly distributed spatially. In order to generate a raster from them or view them as a surface image, interpolation and gridding was required. The Generic Mapping Tools (http://gmt.soest.hawaii.edu), a Linux-based open-source software package widely utilized in the geophysical community for manipulating geographic and Cartesian data sets (Wessel and Smith 1991, 1998), was used for data gridding and interpolation. A DSM with the cell size of 5×5 cm was developed by using the uniformly gridded data sets. The detailed method of gridding and interpolation was described in a previous publication (Wang et al. 2011). The gridding and interpolation process of producing DSM may involve certain errors. Given the high density of the point cloud (more than 5 points/5×5 cm cell), a high-accuracy DSM could be provided. We did not try to pursue the details of the accuracy of DSMs derived from TLS data in this study, which may be slightly different between flat and sloped areas, and between deforested and forested areas. We expect that the overall accuracy of DSMs derived from the TLS data collected for this study is within 3 to 5 cm.

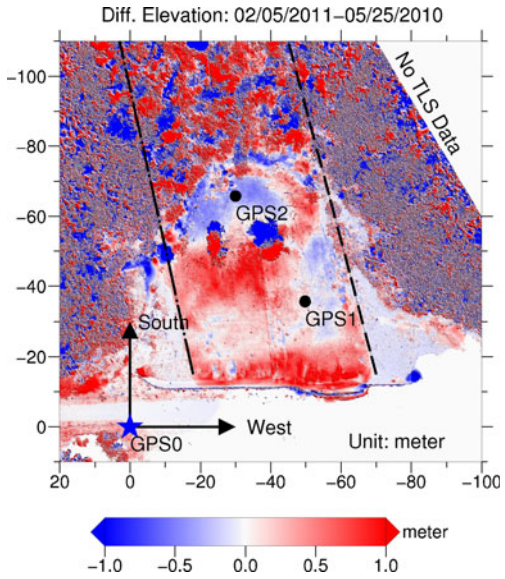

Fig. 11 The changes of elevations derived from two TLS DSMs on 5 February 2011 and 25 May 2010. *Red* and *blue color patterns* indicate increasing and decreasing of elevations of ground surface, respectively. The *dark dashed* and *dotted lines* draw out the superficial margins of the sliding mass in the landslide foot area

Differential TLS

In order to detect the deformation area of the sliding mass, the difference of the first and third DSMs was calculated. DSMs subtractions allow quantifying the variations of topography between two individual TLS surveys: a negative value on the vertical axis corresponds to subsidence; whereas a positive value corresponds to uplift. Figure 11 illustrates the difference of the last DSM (5 February 2011) and the first DSM (25 May 2010), showing the change of topography (elevation) within the 10-month period. The red patterns represent increased elevations, while the blue patterns represent decreased elevations. The deforested lower portion of the landslide is dominated by red patterns with a few light blue zones. The vegetated higher portion is marked by very patchy deep red and blue patterns, which indicate large elevation change caused by the displacement (moving down and forward) of tree canopies and thus serve as a proxy of ground surface movement. The light blue and red interactive color patterns along the left and right sides indicate very slight variations of elevations, which could be caused by the swing of tree canopies. In fact, the light and fine red and blue intervals indicate the stableness of the ground under trees. The color patterns inferred from differential TLS data clearly identify the superficial boundaries of the sliding mass in the deforested area.

Combination of airborne LIDAR, TLS, GPS data, and field observations

Since both ALS data and TLS data sets can be tied to a global coordinate system by the three GPS stations, it is technically easy to combine ALS and TLS data. Figure 12 illustrates the hillshaded bare-earth topographic map derived from ALS and TLS combined digital elevation data. The superficial margins of the whole sliding mass are obtained by combining the upper margins delineated by ALS (Figs. 4 and 7) and lower margins delineated by differential TLS (Fig. 11). The head scarps and both flanks can be clearly identified from the hillshaded topographic map though the resolution of points (ground returns) is pretty low, less than 1 point/3 m² in the head area. The landslide is about 50 m wide and 200 m long. The head is about 60 m higher than the toe area. The overall surface slope of the landslide is about 15°. The toe to head profile indicates that the main head scarp is less than 8 m.

Sliding mechanism

The cross topography profile at the landslide head shown in Fig. 12 indicates that the western flank is about 2 m high. The east and west flanks are essentially parallel and trend towards the N–NW. Our followed field investigations indicate that extensively striated 1–3 m high escarpments in residual soils characterize both sides. The head scarp is on the order of 6–8 m high and also formed on residual soils and highly weathered rock. The western portion of the head scarp is inclined to the N-NE at about 65°. Striations indicate slip directions from N–NW to N–NE at angles from 50° to 70°. Escarpments along both flanks are steeply inclined from 50° to 70° and extensively striated. The flank striations indicate movement from N–NW to N along a basal slip plane at angles 40° near the head, 25° in the middle and 18° in the lower portions of the landslide. The parallelism of west and east flanks and the steep scarps are interpreted as the product of bedrock structural control over the landslide. The occurrence of displaced fractured bedrock in the lower portions of the head scarp also suggests that the landslide movement is controlled by the joint and fractures in the underlying bedrock. This leads to the inference that the basal failure plane lies within the bedrock transition zone below the thick residual soil and colluvium that cover the site.

GPS measurements and TLS data indicate that there was very slight movement during the period between the second TLS survey (August 2010) and the third TLS survey (February 2011) (Table 2).

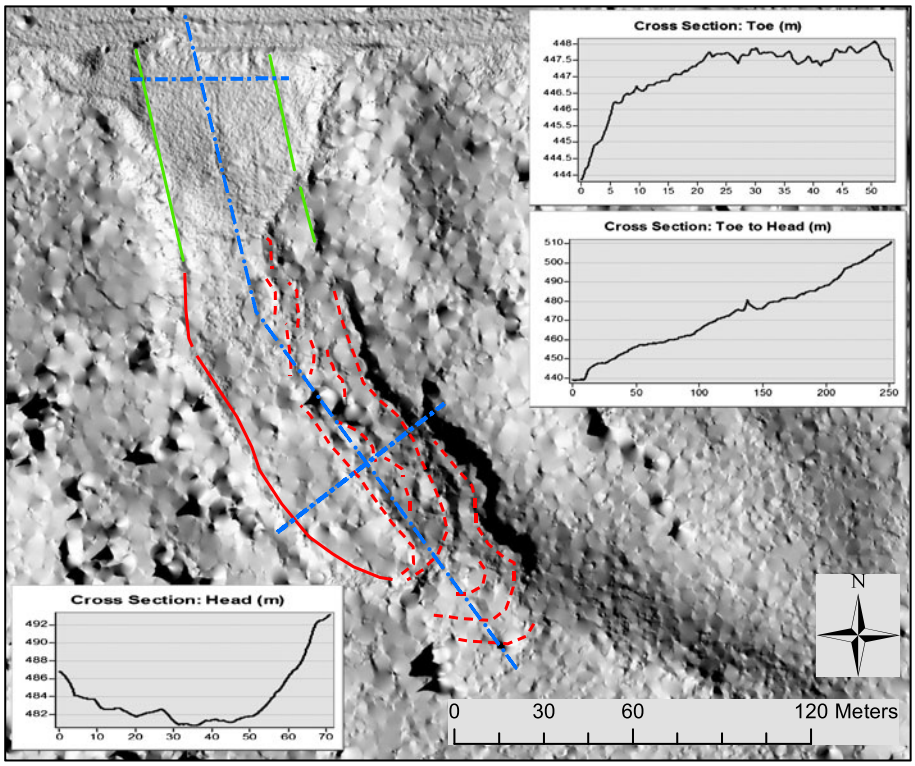

Fig. 12 Hillshaded bare-earth topographic map plotted using ALS and TLS combined elevation data. Three sub-graphics illustrate topographic profiles crossing the landslide toe area, head area, and from the toe to head area. *Green lines* indicate the landslide margins in the foot zone derived from TLS data. *Red lines* indicate landslide margins in the body and head zones derived from ALS data

However, there was certain volume change within the landslide toe area during this period because rainfalls washed away significant soil mass through the ruptured section of the retaining wall. The DSMs derived from the differences between the first and second TLS surveys were used in the following analysis. The total displacements measured by GPS2 on the upper portions of the landslide toe were 3.1, 0.87, and 0.37 m toward north, west, and downward respectively (Table 2). The component displacements can be resolved into a N15W net slip of 3.17 m at an angle of 3.6°. The net slip and low angle are consistent with displacement of the tree that stands between GPS2 and GPS1 seen in the TLS data on Fig. 11. The sub-horizontal slip angle measured at GPS2 is used to constrain the angle of the basal slip plane below the toe to the base of the retaining wall. This angle is consistent with the slip striation data in implying a smoothly curved basal slip plane whose slip angle diminishes to a horizontal surface. Notably, slip striations of 3–5° were observed on the upper portion of the west flank. These low angle striations however, are overprinted by a set of much steeper striations (35–45°) and are believed to be remnants of the earlier development of the landslide. The total displacements at GPS1 are 2.5, 1, and 0.8 m towards north, west, and downward respectively, which can be resolved into a N22W net slip of 2.74 m at angle of 16.8°. The more steeply inclined inferred slip angle, the rising of material behind the wall and the deformation at the top of the wall (Fig. 11) are suggestive of an additional rotational failure surface occurring at the base of the toe behind the retaining wall. Earlier investigations during the final grading behind the wall observed accurate escarpments and uplift behind the wall in this same area. There were also steeper slip striations measured on the extensions of both flanks into the toe of the landslide that ranged from 18° to 30°. These steeper slip striations support the interpretation of a rotational failure mechanism operating in the lower toe portion of the landslide.

Sliding planes

The development of an adequate engineering design to minimize the impact of the landslide requires an accurate model that includes the depth of the landslide mass, which is essential to determine the internal stress distribution. Determining the depth of the basal slip plane is usually accomplished by the emplacement and monitoring of inclinometers within the landslide mass. Limited access to landslides often precludes the emplacement of inclinometers. In such cases geometric models can be constrained by accurate location of the head and toe of the landslide and determination of the slip plane angles as deduced from slip striations on head and flank escarpments.

Interpretations of the depth and form of the basal slip surface of the El Yunque landslide are illustrated on the topographic profile from the toe to head area (Fig. 13). The angles of the sliding plane (failure surface) were inferred from the combination of GPS measurements, topographical features, superficial margins, and field measured slip striation data sets. A model of the internal structure of the landslide was created, by utilizing the ALS data, to develop a topographic profile and accurately locate the head scarp. The TLS and GPS data were used to model deformation in the toe behind the wall. The geologic profile model presented in Fig. 13 constrains the primary slip surface to initiate at a 60° angle at the ALS delineated head scarp and terminate on a flat plane behind

Table 2 Relative positions of three GPS antennas during TLS surveys

TLS survey	Date	GPS0			GPS1 (m)			GPS2 (m)		
		EW	NS	Vertical	EW	NS	Vertical	EW	NS	Vertical
First TLS survey	25 May 2010	0	0	0	−49.84	−35.77	10.06	−30.00	−65.87	18.63
Second TLS survey	24 August 2010	0	0	0	−50.84	−33.29	9.28	−30.87	−62.68	18.26
Third TLS survey	5 February 2011	0	0	0	−50.86	−33.25	9.19	−30.88	−62.61	18.20
Displacement					−1.02	2.52	−0.87	−0.88	3.26	−0.43

the base of the wall at the elevation of the road. The angles derived from the striation data were established in position along the profile from the head scarp plane to the toe and a smoothly curved surface was drawn to conform to the data (Fig. 13, red curved lines). The occurrence of additional scarps and slip planes within the landslide were inferred from field observations, the point cloud density and intensity images (Fig. 4) and the TLS-GPS data. The total volume of the landslide based on area above the modeled basal slip surface and a landslide width of 50 m is estimated to be 219,480 m^3.

The depth to the basal slip plane below the lower portions of the landslide was also estimated using the TLS and GPS data. The decrease in displacements between GPS2 to GPS1 (high to low elevations) and the increase in volume at the toe (Fig. 11) suggested that the displacement of the lower portion of the landslide is driven by the displacement of upper portions of the landslide. This inference was verified by field observations of near meter size displacements all along the head scarp and both flanks. The volumetric change of the sliding mass in the foot area was calculated by the difference between the two DSM models derived from two TLS surveys. The increase in volume of the landslide foot area between the second and first TLS surveys was about 685 m^3 (Wang et al. 2011). The increased volume is considered to represent the soil mass transferred from the upper portions to lower toe portions of the landslide during the period between the two TLS surveys. We used the 3.2-m displacement of GPS2, 50-m width of the sliding mass (see Figs. 11 and 12), and net volume increase of 685 m^3 at the toe, to estimate the depth of the basal slip surface below GPS2 at about 4.3 m. A model of the basal slip surface constrained to 4.3 m depth and a 3° angle below GPS2 and to terminate at the ALS defined head scarp is illustrated as a dotted curved line on Fig. 13. The inferred slide plane angle is not consistent with striation data and remains very low throughout most

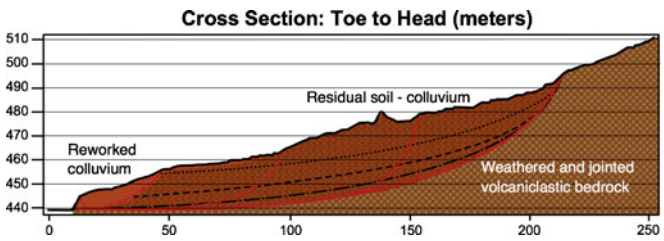

Fig. 13 A sketch showing slide planes (*red curved lines*) of the landslide inferred from the integration of GPS measurements, LIDAR data, and field measurements of slip striations and dip angles observed on both flanks and head scarps. The *dark lines* represent assumed slip planes based on different scenarios. The details are explained in the "Sliding planes"

of the landslide, as does the depth. The total volume of the landslide estimated from this model is only 106,290 m^3. Underestimation of the depth and volume of the landslide is a consequence of assuming the entire toe mass was displaced the 3.2 m measured in GPS2. Both the GPS1 data and the TLS data indicate inhomogeneous deformation (displacement) within the landslide foot area. Figure 11 shows that the tree to the east of GPS2 was only displaced about half of the distance of the tree between GPS2 and GPS1. Differential displacement within the toe is expected if the landslide is moving as an earth flow where there is greater displacement in the center and less along the sides and bottom of the toe mass. Also, the greater amount and direction of displacement of GPS2 and GPS1 were caused by the deformation and eventual rupture of a section of the retaining wall. More GPS instruments and/or TLS markers distributed within the toe mass may have allowed for a better determination of the average displacement of the toe mass. The depth to the basal slip surface calculated using an average displacement of 1 m. A slip surface constrained to this depth and 3° angle below the toe is shown as a dashed line on Fig. 13. This modeled slip surface while similar in form to geometric model is 6 m shallower and underestimates the volume of the landslide at 156,150 m^3. Another slip surface model based solely on the ALS data was modeled with the only constraints being that the slip surface end in a 3° angle at the base of the retaining wall and to initiate at a steep 60° angle at the head scarp. This model, as shown with a dashed–dotted curve on Fig. 13, is similar in shape and depth to the geometric model generated using the slip striations and provides reasonable estimates of 18 m for the depth and 185,675 m^3 for the volume of the slide. A displacement of about 0.75 m of the upper slide mass is suggested by using the estimated depth of about 18 m from the model and the 685 m^3 TLS derived volume change. The significance of this is that the integrated ALS, TLS, and GPS data and some reasonable assumptions about the shape of landslide slip surfaces have allowed us to delineate the size and extent of the landslide, estimate its depth and volume, as well as recognize recent activity.

Discussion and conclusions

We estimate that the total volume of the current sliding mass to be over 200,000 m^3 based on the 3D geometry of the sliding mass derived from this study. The step scarps in the east flank and head area shown in the DTMs (Figs. 7 and 12) indicate that the landslide is still retreating, which was also verified by our field investigations. The surprising result of this study is that despite the 0.75 m displacement of this huge landslide mass, most of the retaining wall remains intact. The TLS data demonstrated that the displaced landslide mass is piling up behind the retaining wall. The TLS and

GPS data indicate that the rupture of the western section of the wall was caused by a localized concentration of displacement and a rotational failure mechanism at the toe. Our findings suggest that it may be possible to repair the ruptured portion of the wall and, with routine maintenance at the toe, prevent failure along the remainder of the wall. A successful rehabilitation design for the retaining wall will require that our findings be augmented by a detailed geotechnical investigation with adequate subsurface data from borings and inclinometers within the accessible toe portion of the landslide.

LIDAR technology and modern software have provided practicing geologists a new way to map the Earth's surface and land cover at unprecedented spatial resolution and accuracy over large areas, which is opening new ways of investigating landslide phenomena. TLS has high resolution and accuracy, but very limited spatial coverage. ALS has somewhat lower resolution and accuracy, but basically unlimited spatial coverage. TLS complements ALS by providing high-accuracy and high-resolution data for study specific areas that cannot be addressed by ALS alone. The ability of ALS to acquiring densely sampled bare-earth elevations beneath forest canopies is particularly critical to studying landslide and other topographic features hidden in forest areas which have traditionally been difficult to study with remote sensing and onsite techniques. The portability and low-cost advantages of TLS make it is feasible to conduct repeated surveys and study the deformation of currently active landslides. Many key scientific questions are setting on high-resolution and high-accuracy topographic data, as well as point cloud density and intensity data. It takes creative and well-designed data acquisition procedures and data filtering techniques to meet these standards. Integration of ALS and TLS data will greatly increase both data density and accuracy, which will, in turn, create new challenges in data processing and management, but also new research opportunities.

Acknowledgments

The airborne LIDAR data were collected by NCALM engineers Michael Sartori, Abhinav Singhania, and Juan Fernandez. We appreciate their efforts in the field as well as their assistance in airborne LIDAR data processing. Graduate students Felix O. Rivera and Leila Joyce and undergraduates Arlenys Ramirez Rivera, Fernando Martinez, and Francis Hernández at the University of Puerto Rico Mayaguez campus assisted in field surveys. We appreciate their hard work in the field. This study was funded by a NSF CAREER Award (EAR-1229278), and the TLS equipment was provided by UNAVCO.

References

Abellan A, Vilaplana JM, Martinez J (2006) Application of a long-range terrestrial laser scanner to a detailed rockfall study at Vall de Nuria (Eastern Pyrenees, Spain). Eng Geol 88:136–148. doi:10.1016/j.enggeo.2006.09.012

Abellan A, Jaboyedoff M, Oppikofer T, Vilaplana JM (2009) Detection of millimetric deformation using a terrestrial laser scanner: experiment and application to rockfall event. Nat Hazards Earth Syst Sci 9:365–372. doi:10.5194/nhess-9-365-2009

Adams JC, Chandler JH (2002) Evaluation of LIDAR and medium scale photogrammetry for detecting soft-cliff coastal change. Photogramm Record 17(99):405–418

Ardizzone F, Cardinali M, Galli M, Guzzetti F, Reichenbach P (2007) Identification and mapping of recent rainfall-induced landslides using elevation data collected by airborne LIDAR. Nat Hazards Earth Syst Sci 7:637–650. doi:10.5194/nhess-7-637-2007

Bevis M, Hudnut K, Sanchez R, Toth C, Grejner-Brzezinska D, Kendrick E, Caccamise D, Raleigh D, Zhou H, Shan S, Shindle W, Yong A, Harvey J, Borsa A, Ayoub F, Elliot B, Shrestha R, Carter B, Sartori M, Phillips D, Coloma F, Stark K (2005) The B4Project: scanning the San Andreas and San Jacinto fault zones. Eos Trans AGU 86 (52) Fall Meet Suppl, Abstract H34B-01

Booth AM, Roering JJ, Perron JT (2009) Automated landslide mapping using spectral analysis and high resolution topographic data: Puget Sound lowlands, Washington, and Portland Hills, Oregon. Geomorphology 109:132–147. doi:10.1016/j.geomorph.2009.02.027

Bowen ZH, Waltermire RG (2002) Evaluation of light detection and ranging (LIDAR) for measuring river corridor topography. J Am Water Resour Assoc 38(1):33–41

Carter WE, Shrestha R, Tuell D, Bloomquist D, Sartori M (2001) Airborne laser swath mapping shines new light on earth's topography. Eos Trans Am Geophys Union 82 (46):549–555

Carter WE, Shrestha R, Slatton KC (2007) Geodetic laser scanning. Phys Today, December, 41-42

Corsini A, Cervi F, Daehne A, Ronchetti F (2009) Coupling geomorphic field observation and LIDAR derivatives to map complex landslides. In: Malet JP, Remaître A, Bogaard T (eds) Landslides processes—from geomorphologic mapping to dynamic modelling. Proceedings of the landslide processes conference. CERG Editions, Strasbourg, pp 15–18, ISBN 2-9518317-1-4

Delano HL, Braun DD (2007) PAMAP LIDAR-based elevation data: a new tool for geologic and hazard mapping in Pennsylvania. Geol Soc Am Abstr Programs 39(6):167

Derron MH, Jaboyedoff M (2010) Preface to the special issue. In: LIDAR and DEM techniques for landslides monitoring and characterization. Nat Hazards Earth Syst Sci 10:1877–1879

Donoghue DNM, Watt PJ, Cox NJ, Wilson J (2007) Remote sensing of species mixtures in conifer plantations using LIDAR height and intensity data. Remote Sens Environ 110 (4):509–522

Dunning S, Massey C, Rosser N (2009) Structural and geomorphological features of landslides in the Bhutan Himalaya derived from terrestrial laser scanning. Geomorphology 103:17–29. doi:10.1016/j.geomorph.2008.04.013

Falls JN, Wills CJ, Hardin BC (2004) Utility of LIDAR survey for landslide mapping of the Highway 299 corridor, Humboldt County, California. Geol Soc Am Abstr Programs 36 (5):331

Fanti R, Gigli G, Lombardi L, Tapete D, Canuti P (2012) Terrestrial laser scanning for rockfall stability analysis in the cultural heritage site of Pitigliano (Italy). Landslides. doi:10.1007/s10346-012-0329-5

Glenn NF, Streutker DR, Chadwick DJ, Thackray GD, Dorsch SJ (2005) Analysis of LIDAR derived topographic information characterizing and differentiating landslide morphology and activity. Geomorphology 73(1–2):131–148. doi:10.1016/j.geomorph.2005.07.006

Glenn NF, Streuker DR, Chadwick DJ, Thackray GD, Dorsch SJ (2006) Analysis of LIDAR derived topographic information for characterizing and differentiating landslide morphology and activity. Geomorphology 73:131–148

Habib A (2008) Accuracy, quality assurance and quality control of LIDAR data, Chap 9. In: Shan J, Toth CK (eds) Topographic laser ranging and scanning: principles and processing. CRC Press, Boca Raton, pp. 269–294

Hasegawa H (2006) Evaluations of LIDAR reflectance amplitude sensitivity towards land cover conditions. Bull Geogr Surv Inst 53:43–50

Haugerud RA, Harding DJ, Johnson SY, Harless JL, Weaver CS, Sherrod BL (2003) High-resolution LIDAR topography of the Puget Lowland, Washington—a Bonanza for earth science. GSA Today 13:4–10

Heritage GL, Large ARG (2009) Fundamentals of laser scanning. In: Heritage GL, Large ARG (eds) Laser scanning for the environmental sciences. Wiley-Blackwell, Chichester

Hodgson ME, Bresnahan P (2004) Accuracy of airborne LIDAR-derived elevation: empirical assessment and error budget. Photogramm Eng Remote Sens 70(3):331–339

Hodgson ME, Jensen JR, Schmidt L, Schill S, Davis B (2003) An evaluation of LIDAR- and IFSAR-derived digital elevation models in leaf-on conditions with USGS level 1 and level 2 DEMs. Remote Sens Environ 84:295–308

Jaboyedoff M, Pedrazzini A, Horton P, Loye A, Surace I (2008) Preliminary slope mass movements susceptibility mapping using LIDAR DEM. In: Proceedings of 61th Canadian geotechnical conference, pp. 419–426

Jaboyedoff M, Oppikofer T, Locat A, Locat J, Turmel D, Robitaille D, Demers D, Locat P (2009) Use of ground-based LIDAR for the analysis of retrogressive landslides in sensitive clay and of rotational landslides in river banks. Can Geotech J 46:1379–1390. doi:10.1139/T09-073

Jaboyedoff M, Oppikofer T, Abellán A, Derron MH, Loye A, Metzger R, Pedrazzini A (2012) Use of LIDAR in landslide investigations: a review. Nat Hazards 61:5–28. doi:10.1007/s11069-010-9634-2

Kaasalainen S, Ahokas E, Hyyppa J, Suomalainen J (2005) Study of surface brightness from backscattered laser intensity: calibration of laser data. Remote Sens Lett 2 (3):255–259

Kasperski J, Delacourt C, Allemand P, Potherat P, Jaud M, Varrel E (2010) Application of a terrestrial laser scanner (TLS) to the study of the Séchilienne Landslide (Isère, France). Remote Sens 2:2785–2802. doi:10.3390/rs122785

Mazzarini F, Pareschi M, Favalli M, Isola I, Tarquini S, Boschi E (2007) Lava flow identification and aging by means of lidar intensity: Mount Etna case. J Geophys Res 112(B2): doi:10.1029/2005JB004166. ISSN: 0148-0227

Razak KA, Straatsma MW, van Westen CJ, Malet JP, de Jong SM (2011) Airborne laser scanning of forested landslides characterization: terrain model quality and visualization. Geomorphology 126:186–200. doi:10.1016/j.geomorph.2010.11.003

Shan J, Toth K (2008) Topographic laser ranging and scanning: principles and processing. CRC Press, London

Shrestha RL, Carter WE, Lee M, Finer P, Sartori M (1999) Airborne laser swath mapping: accuracy assessment for surveying and mapping applications. J Am Congr Surv Mapp 59(2):83–94

Shrestha RL, Carter WE, Slatton KC, Dietrich W (2007) "Research quality" airborne laser swath mapping: the defining factors, Ver.1.2, white paper. Available at http://ncalm.berkeley.edu/reports/NCALM_WhitePaper_v1.2.pdf

Slatton KC, Carter WE, Shrestha RL, Dietrich W (2007) Airborne laser swath mapping: achieving the resolution and accuracy required for geosurficial research. Geophys Res Lett 34:L23S10. doi:10.1029/2007GL031939

Teza G, Galgaro A, Zaltron N, Genevois R (2007) Terrestrial laser scanner to detect landslide displacement fields: a new approach. Int J Remote Sens 28:3425–3446. doi:10.1080/01431160601024234

Teza G, Pesci A, Genevois R, Galgaro A (2008) Characterization of landslide ground surface kinematics from terrestrial laser scanning and strain field computation. Geomorphology 97:424–437. doi:10.1016/j.geomorph.2007.09.003

Travelletti J, Oppikofer T, Delacourt C, Malet J, Jaboyedoff M (2009) Monitoring landslide displacements during a controlled rain experiment using a long-range terrestrial laser scanning (TLS). Int Arch Photogramm Remote Sens 37(B5):485–490

Van Den Eeckhaut M, Poesen J, Verstraeten G, Vanacker V, Moeyersons J, Nyssen J, Van Beek LPH, Vandekerckhove L (2007) Use of LIDAR-derived images for mapping old landslides under forest. Earth Surf Process Landforms 32(5):754–769. doi:10.1002/esp.1417

Wang G, Soler T (2012) OPUS for horizontal subcentimeter-accuracy landslide monitoring: case study in the Puerto Rico and virgin islands region. J Surv Eng 138(3):143–153. doi:10.1061/(ASCE)SU.1943-5428.0000079

Wang G, Phillips D, Joyce J, Rivera FO (2011) The integration of TLS and continuous GPS to study landslide deformation: a case study in Puerto Rico. J Geodetic Sci 1(1):25–34. doi:10.2478/v10156-010-0004-5

Wehr A, Lohr U (1999) Airborne laser scanning—an introduction and overview. ISPRS J Photogramm Remote Sens 54:68–82. doi:10.1016/S0924-2716(99)00011-8

Wessel P, Smith WHF (1991) Free software helps map and display data. EOS Trans AGU 72:441

Wessel P, Smith WHF (1998) New, improved version of the Generic Mapping Tools released. EOS Trans AGU 79:579

Wooten RM, Latham RS, Witt AC, Douglas TJ, Gillon KA, Fuemmeler SJ, Bauer JB, Nickerson JG, Reid JC (2007) Landslide hazard mapping in North Carolina—geology in the interest of public safety and informed decision making. Geol Soc Am Abstr Programs 39(2):76

G. Wang (✉) · R. Shrestha
Department of Earth and Atmospheric Sciences,
University of Houston,
Houston, TX, USA
e-mail: gwang@uh.edu

G. Wang · R. Shrestha · W. Carter
Department of Civil and Environmental Engineering,
University of Houston,
Houston, TX, USA

J. Joyce
Department of Geology,
University of Puerto Rico at Mayaguez,
Mayaguez, PR, USA

D. Phillips
UNAVCO,
Boulder, CO, USA

G. Wang · R. Shrestha · W. Carter
The National Center for Airborne Laser Mapping (NCALM),
University of Houston,
Houston, TX, USA